Wind responses of Giant Magellan telescope

Benjamin Irarrazaval[a] and Christine Buleri[b] and Matt Johns[a]
[a]GMTO Corporation, 251 S. Lake Ave suite 300, Pasadena, Ca USA 91101
[b]Quartus Engineering, 10251 Vista Sorrento Parkway Suite 250, San Diego, USA 92121

ABSTRACT

The Giant Magellan Telescope (GMT) is 25 meter diameter extremely large ground based infrared/optical telescope being built by an international consortium of universities and research institutions. It will be located at the Las Campanas Observatory in Chile. The GMT primary mirror consists of seven 8.4 meter diameter borosilicate mirror segments. Two seven segment Gregorian secondary mirror systems will be built; an Adaptive Secondary Mirror (ASM) to support adaptive optics modes and a Fast-steering Secondary Mirror (FSM) with monolithic segments to support natural seeing modes when the ASM is being serviced.

Wind excitation results in static deformation and vibration in the telescope structure that affects alignment and image jitter performance. The telescope mount will reject static and lower frequency windshake, while each of the Fast-steering Secondary Mirror (FSM) segments will be used to compensate for the higher frequency wind-shake, up to 20 Hz. Using a finite element model of the GMT, along with CFD modeling of the wind loading on the telescope structure, wind excitation scenarios were created to study the performance of the FSM and telescope against wind-induced jitter. A description of the models, methodology and results of the analyses are presented.

INTRODUCTION

The GMT is a 25 m altitude-azimuth telescope designed for operation over the wavelength range 320 nm to 25 μm. The optical system uses a segmented primary mirror composed of 8.4 m diameter circular segments. The segments are arranged in a hexagonal array of six segments surrounding a center segment that share a common parent optical surface. Seven 1.05 meter secondary mirror segments are conjugated 1:1 with the primary segments. The alt-az mount provides complete access to the sky above 30 deg elevation angle.

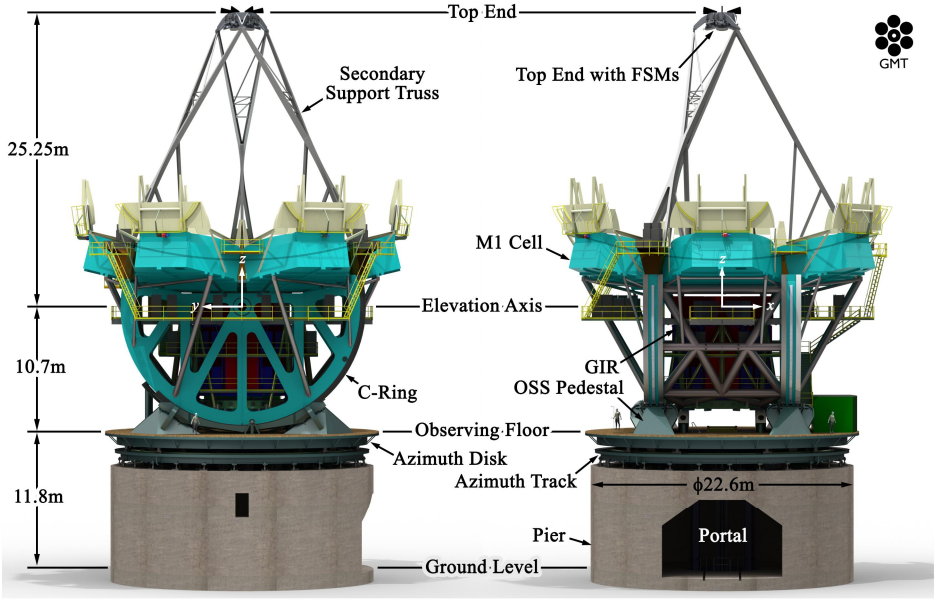

Figure 1. Telescope structure and description of subassemblies.

Modeling, Systems Engineering, and Project Management for Astronomy VI,
edited by George Z. Angeli, Philippe Dierickx, Proc. of SPIE Vol. 9150, 915022
 · doi: 10.1117/12.2057130

The mount uses direct linear drives and hydrostatic bearings for both the azimuth and elevation axes. The drives consist of forcer heads that apply an electromagnetic force to curved magnet tracks, producing a rotating torque over each axis. The azimuth axis driver is composed of four forcer heads mounted on the azimuth structure underneath each OSS pedestal, and a 18.9 meter diameter circular magnet track mounted on the top of the azimuth track, right between the runner bearing surfaces for the axial bearings. The elevation drive is composed by two magnet tracks mounted on the perimeters of the C-Rings between the runner bearing surfaces for the radial bearings, and four forcers attached to the azimuth disk with one forcer atop each pedestal at a radius of 10.2 meters from the elevation axis. The maximum torque for the drives are driven by the following factors, acceleration times, wind load and drag forces of the bearings. A total of 275 kNm is required for the elevation axis and 250kNm for the Azimuth Axis. Under nominal tracking conditions it is expected that the required torque will not exceed 30kNm. The telescope will be shielded from the wind by the enclosure. To minimise dome seeing the enclosure is fitted with 114 vent gates (4x6 meters). The opening of the vent gates can be controlled independently in 25% aperture increments.

The telescope main axes provide the principal means for tracking astronomical objects across the sky. The closed-loop servo response of the main drives is not; however, fast enough to deal with tracking errors that occur faster than about 2 Hz. The secondary mirrors (FSM or ASM) are used to correct higher frequency tracking errors (windshake, structure vibration, and main axis servo jitter) up to the mechanical limitations of the mirrors and telescope structure.

The Acquisition, Guide and Wavefront Sensor (AGWS) assembly uses guide stars to measure tracking errors which are then sent to the mount control in the Telescope Control System (TCS). The TCS analyzes the input and sends the appropriate demands to the mount and FSM/ASM. Separate terms in the Image Quality Budget apply to the AGWS, FSM, and ASM. The systems do interact, however, and place limitations on each other. The AGWS sets limits on the update-rate of the FSM/ASM in order for the AGWS to meet its Sky Coverage requirements. The Sky Coverage requirement limits the minimum exposure time, directly affecting bandwidth of the system. These limitations directly affect the telescope tracking performance. Details of the design of the GMT can be found at Design of the Giant Magellan Telescope[1].

This paper summarizes the analysis of the wind disturbances over the mount with the tip/tilt control under various wind scenarios and compares the results with the Natural Seeing Image Quality Budget[2].

2 WINDSHAKE REQUIREMENTS

Allowable tracking-error residuals are allocated from the GMT Natural Seeing Image Quality Budget. The total image motion allowed by effects of the wind over the mount and its optical elements is 0.109 arcsec 80% Encircled Energy (EE80), this value can be translated to an image motion at the focal plane of 0.043 arcsec RMS. Another budget of concern is the maximum centroid calculation error, value dominated by the signal to noise ratio of the fast tip/tilt camera. The budget allocated to the centroid calculation error is 0.1 arcsec EE80, which translate in 0.039 arcsec RMS in the focal plane.

3 MODELING PROCESS

The diagram in Figure 2 shows the components associated with the dynamic behavior of the focal plane image motion as a response to several inputs. In the diagram, four inputs can be identified as: axis references from the pointing kernel, the windshake, encoder noise and centroid calculation noise. The primary output is the focal plane image motion but also the axis angles can be obtained from here.

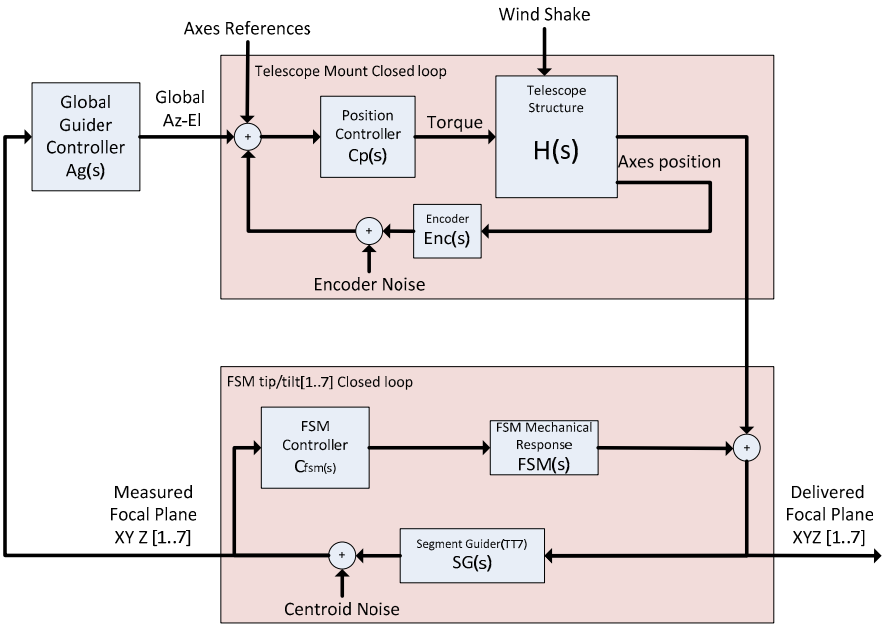

Figure 2. Simplified global control loop for tracking

In the block diagram, the telescope structure block represents the opto-mechanical focal-plane motion response to torque on each axis and wind over the whole structure. The telescope structure output is the residual focal-plane X and Y image motion after correction by the mount control loops for the seven sub apertures. The position controller block represents models of the control algorithm and the drive response. The output of this block is pure torque over the two axes of the mount. Each axis loop is closed locally by the tape encoders, the tape encoders are closely located to the force application points of the mount drives, and therefore their response are assumed collocated. The model of the position controller follows a standard PID controller. The encoders were modeled as simple latency devices.

The residual focal-plane image motion can be corrected at higher bandwidth (than the mount) by the tip/tilt control system. This system is composed by a segment guider (TT7) that will provide X and Y centroid information for each of the seven sub apertures. The FSM mechanical response represents the open loop mechanical response of the FSM structure. The X and Y measured signals of the focal plane are filtered and averaged by the guider controller, which produces global corrections for the mount. .

3.1 Telescope structural model

A finite element model (FEM) of the preliminary telescope design was created to analyze telescope performance when subjected to disturbances associated with static gravity deformation, wind buffeting, and seismic events. The model includes the pier with a fixed boundary condition where the pier interfaces with the ground. When necessary, lumped mass representations of components are used to model the rigid body mass properties. This is typical for instruments and other components where mass allocation is provided in the specifications, but the designs are not complete. Counterbalance weights and non-structural mass are applied at defined locations to maintain the center of gravity for the elevation structure at the elevation axis.

Many structure components are constructed of welded steel plate. These components are represented in the FEM with quadrilateral and triangular plate elements with appropriate thickness properties. Most stiffeners, tubes, and beams are represented using one dimensional beam elements with appropriate cross-section properties. Three dimensional solid elements are used to model the pier, as well as some small local blocks on the M1 Outer cells that interface with the outer cell-bracing structure. The linear stiffnesses associated with hydrostatic bearings, drives, Gregorian instrument rotator (GIR) bearings, FSM tip/tilt actuators, and the M2 positioner actuators are modeled using linear spring elements. Components such as instruments, secondary mirror subassemblies, the M3 subassembly and counterbalance masses are

modeled using concentrated mass elements. Rigid elements are used where necessary to provide rigid offsets from flexible structural elements, mostly to provide the correct geometry at interfaces so that the loads at these interfaces are spread out appropriately to their attachment points.

Line of sight sensitivity equations are included in the FEM using multi-point constraint (MPC) equations. MPC equations sum a collection of individual nodal displacements or rotations multiplied by a scalar value. In this manner, the effect of displacement or rotation of each optic along the beam path is added to the total focal plane image motion and focus shift. Equations are included for each of the seven sub apertures along with a weighted mean for the Direct Gregorian Narrow Field (DGNF),. These equations maintain phase information when included in a random vibration solution, such as the solution used for wind dynamic analysis.

The analytical solver for the finite element analyses described in this section was Nastran. NX/Nastran 8.5 was used for all static, modal, and random vibration analyses. Femap 11.0 was used as the pre- and post-processor of model information and results. Star-CCM was used for CFD results post-processing.

Using the FEA model, free rotor frequency responses are computed, providing data to develop continuous time models in MATLAB. Models outputs are the rotational angles of azimuth and elevation, along with the X and Y motions of each sub aperture at the focal plane. The response of the angular motion about the rotation axes were obtained at the force application point, not at the location of the tape encoders, as explained above, due to their location, they are considered to provide a collocated response to the drive torque.

3.1.1 Azimuth frequency response

The Azimuth collocated response and the focal plane image motion response to torque are presented in Figure 3. The collocated response presents the following characteristics; at low frequencies, it can be observed that there is a double pole at 0 Hz associated to an inertial mass of 8.34e+7 kgm^2. This is consistent with the inertial mass of the azimuth including the OSS within 1.7%. The first zero is at 5.46 Hz and the first-resonant pole is at 5.70 Hz. This resonant pole is associated with the torsion of the GIR out of phase. The second-resonant pole at 8.48 Hz is associated with the secondary support truss twisting. All of the mode responses are associated with damping coefficients close to 2%, which is the value used in the FEM for the structural elements. For modeling of the wind disturbance performance,

the response has been model with an analytical function Haz(s) in the Laplace plane. The Bode diagram of Haz(s) is plotted in blue on the Figure 3.

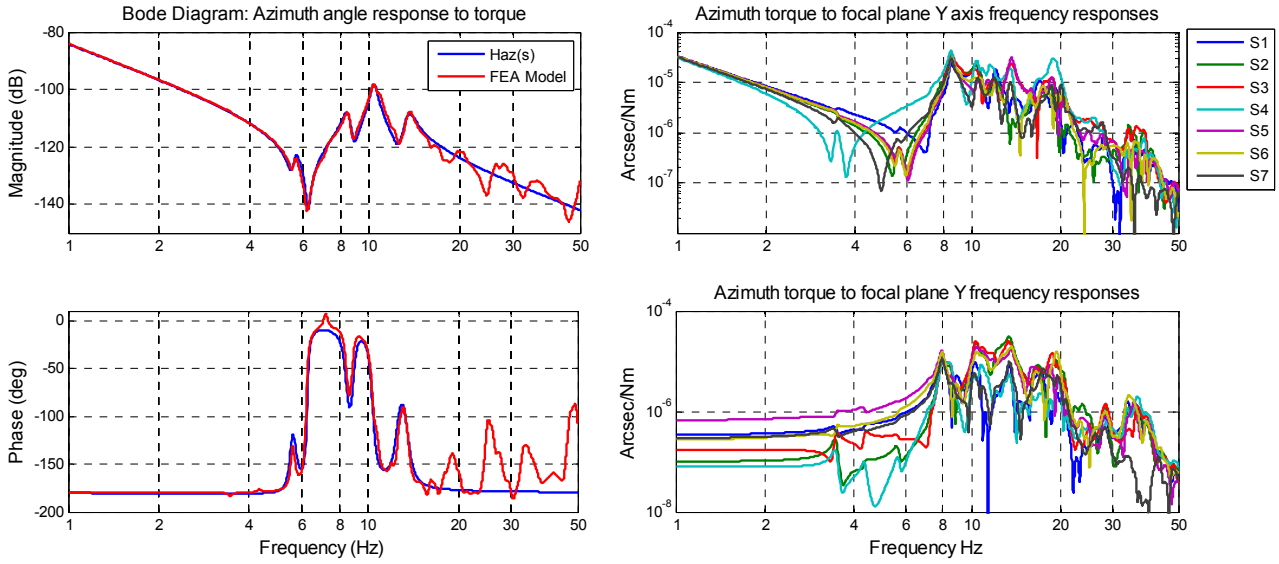

Figure 3. FEM collocated and focal plane responses to motor force at azimuth drive locations

It is important to note that the first mode of the telescope structure is barely excited in the frequency response at the focal plane, see the right side of the plots. The same can be said for the second mode, the fore and aft mode of the elevation axis. The explanation for this might reside in the orthogonality of the modes to the actuation torque at the azimuth disk. The next two natural modes are associated with torsion of the GIR and M2, they are also absent in the response because Line of Sight equations are insensitive to rotation about the optical axis. The bandwidth of the azimuth axis closed loop should be limited to less than half of 5.70 Hz to ensure this mode is not excited. The focal plane responses at the right side of Figure 3 are used to compute the focal plane image motion as a response of the mount to windshake.

3.1.2 Elevation Axis Frequency Response

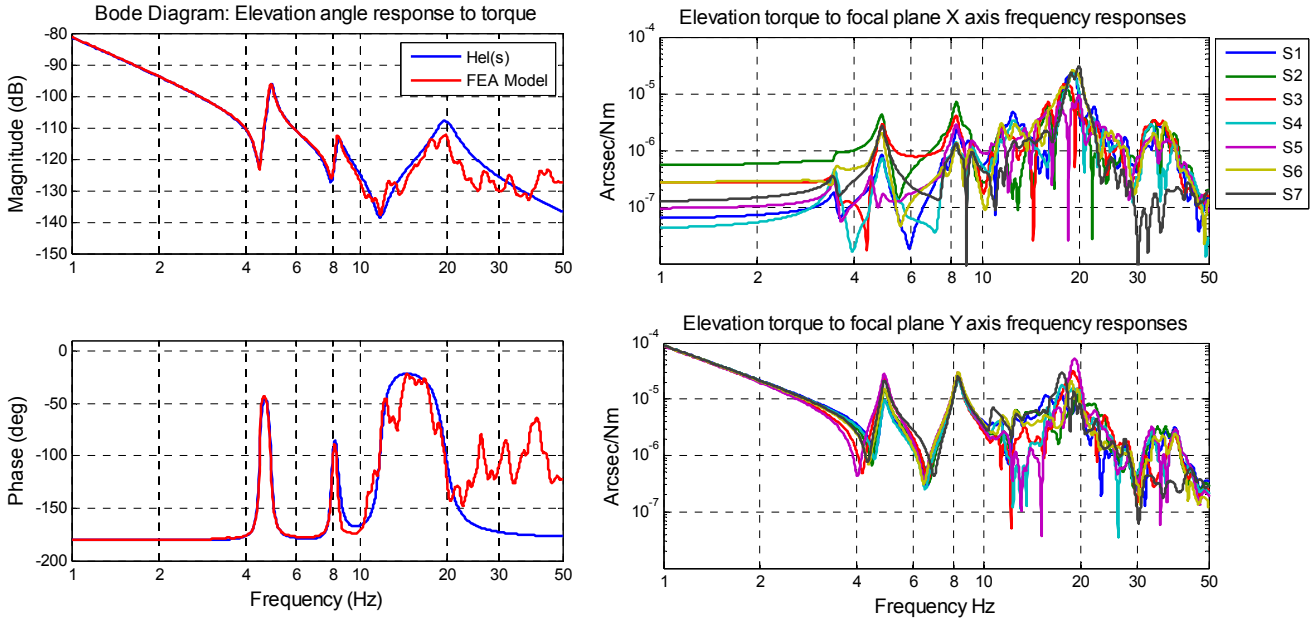

Figure 4. FEM Collocated Responses to Motor Force at Elevation Drive Locations

The elevation axis presents the following characteristics: At low frequencies, it can be observed a behavior of a double pole at 0 Hz associated to an inertial mass of 5.96e7 kgm^2, which is consistent with the inertial mass of the OSS, within 1.2%. The first zero is at 4.47 Hz and the first-resonant pole is at 4.9 Hz. This resonant pole is associated to the secondary support truss first fore and aft mode shape. The second-resonant pole at 8.35 Hz corresponds to the second fore and aft mode shape. The focal-plane image motion follows the axis-angle response up to 5 Hz. The resonant mode at 8.35 Hz is amplified. This amplification is contributed mainly by the translation and rotation of M2. The bandwidth of the system should be limited to less than half of the 4.9Hz that represents the first trusses fore and aft mode. For modeling the wind disturbance performance the response has been model with an analytical function Hel(s) in the Laplace plane. The Bode diagram of Hel(s) is plotted in blue on the Figure 4.

3.2 Position controller and tuning

The position controller model used for all of the frequency domain analysis is:

$$\mathbf{Cp(s)} = \frac{\mathbf{K_d s^2 + K_d K_p s + K_d K_i}}{\mathbf{s}}$$

The inertial mass of the axis, plus gain and phase margins were used to derive the nominal tuning parameters for a PID controller. Since the frequency bandwidth of the closed loop will be tuned to about 2 Hz, the model for the plant and controller can be further simplified to $L_{tune}(s)$, for tuning purposes only.

$$L_{tune}(s) = \frac{Kd(s^2 + Kps + Ki)}{Im_{axis}\, s^3}$$

Using the tuning parameters Phase Margin (PM), Gain Margin (GM) and the frequency bandwidth (Fc), the gains are calculated for L_{tune} as follows:

Fc = 2.0 Hz Elevation and 2.5 Hz Azimuth

PM = 50 degrees

GM = 12 dB = $10^{12/20}$

$$CPM = \frac{1}{\tan\left(PM/2\pi\right)} \qquad Ki = \frac{4\pi^2 Fc^2 CPM}{\mathrm{GM}\sqrt{1 + CPM^2}} \qquad Kd = \frac{GM * J * Ki * 2\pi Fc}{CPM * (4\pi^2 Fc^2 - \mathrm{Ki})} \qquad Kp = \frac{CPM * (4\pi^2 Fc^2 - \mathrm{Ki})}{2\pi Fc}$$

3.3 Model of the motor and motor controller

The motors of the azimuth axis and the elevation axis can be modeled as follows:

$$\mathbf{M(s)} = \frac{\mathbf{2\pi 100 e^{-\Delta ts}}}{\mathbf{s + 2\pi 100}}$$

3.4 Encoder model

For the frequency domain windshake and noise performance, the encoder was simulated as a unity gain with a transport delay of Δts.

$$Enc(s) = e^{-\Delta ts}$$

3.5 Closed loop transfer functions.

For the purpose of this paper only one transfer closed loop transfer function is of interest, the sensitivity to input disturbance, also called Sio(s), and it is computed as follows.

$$S_{io}(s) = \frac{\mathrm{H(s)}}{1 + \mathrm{Cp(s)} * \mathrm{M(s)} * \mathrm{H(s)} * \mathrm{Enc(s)}}$$

Each of these functions Sio, H, Cp and Enc correspond to a particular function for each axis. Figure 5 presents the bode magnitude of the sensitivity of the wind disturbance.

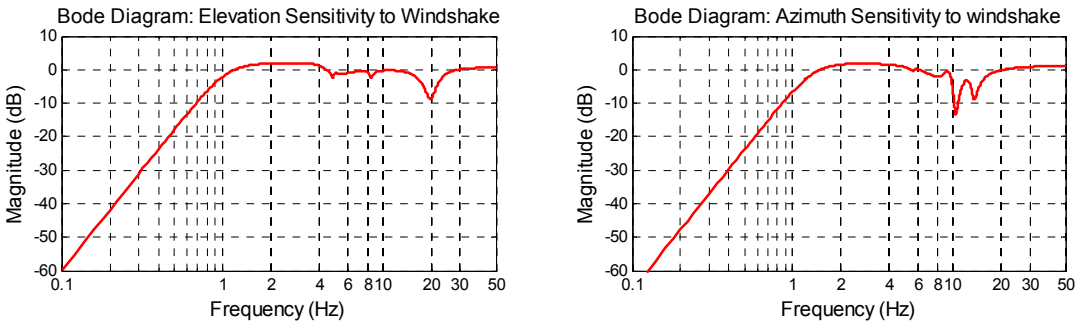

Figure 5. Bode magnitude of sensitivity to wind disturbance

For completeness the transfer function of the reference to the angular output, T(s) is computed as:

$$T(s) = \frac{\mathrm{Cp(s)} * \mathrm{M(s)} * \mathrm{H(s)}}{1 + \mathrm{Cp(s)} * \mathrm{M(s)} * \mathrm{H(s)} * \mathrm{Enc(s)}}$$

3.6 Tip/tilt control model

The goal of the FSM is to operate in closed loop with the tip/tilt segment guider to reject image motion due to windshake. The local FSM closed-loop diagram is presented in Figure 6, this is a subset of Figure 2.

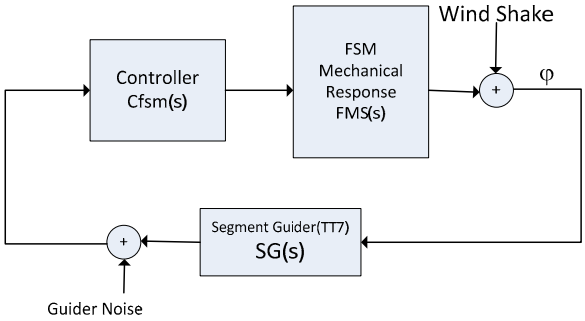

Figure 6. Control diagram of FSM loop

Each of the blocks possesses a unique transfer function expressed in the Laplace variable.

- Guider Centroid Sensor: SG(s)
- Motion Controller: Cfsm(s)
- Fast Steering Mirror: FSM(s)

The following signal is considered input to the system.

- Noise from Guider signal: $G_{noise}(s)$
- Wind induce image motion at the focal plane.(Wind shake)
- The following signals are considered output states of the system.

- Focal-plane angular position: $\varphi(s)$

The transfer function So(s) is the resultant transfer function between the windshake disturbance and the focal-plane motion $\varphi(s)$:

$$\mathrm{So(s)} = \frac{\varphi(s)}{\mathrm{Ws(s)}} = \frac{1}{1 + SG(s) * FSM(s) * C_{fsm}(s)}$$

In order to get a good rejection of windshake the transfer function needs to be as small as possible while maintaining a stable response.

Due to the discrete nature of the feedback sensor, its low rate and large latency, the So transfer functions (used for the frequency domain analysis) were obtained by time simulations, in Simulink. These transfer functions were obtained for varying updates rates, latencies and integrator gains as explained below.

For the time domain simulations, the segmented guider was modeled as a simple integrator with a gain scaled to the integration time and a reset at the end of each integration time. The controller is a simple design starting with a sample and hold, a discrete integrator and a gain. The block diagram of Figure 7 shows the closed-loop model of the FSM and segment guider.

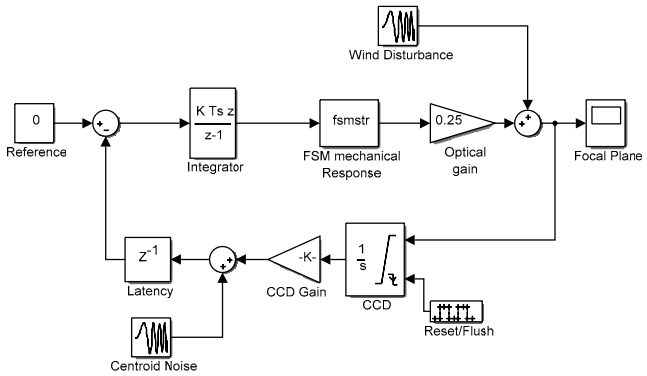

Figure 7 . Simulation Block Diagram of FSM

Without a detailed model of the mechanical response of the tip/tilt mechanism of the FSM, a limited Modal FEA analysis was used to provide the resonant modes of the FSM assembly. Using these modes a frequency response was fitted to the action of the tip/tilt actuators. The Bode diagram represents the angular response to demands of the tip/tilt actuators and is presented in Figure 8. This response considers a fast position control loop embedded in the local controller and is why the gain at low frequencies is 0dB. The FEA models provided a resonant mode of 63 Hz coupled to the axial motion of the tip/tilt actuators. It should be noted that the first mode of the FSM itself is about 40Hz, but it is a torsional mode, highly orthogonal to the tip/tilt actuation and hence is not present in Figure 8.

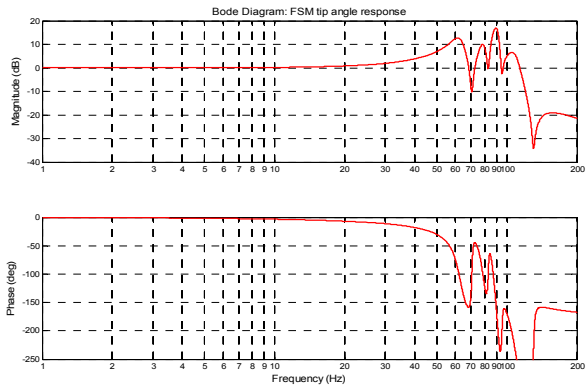

Figure 8. Frequency response of FSM tip/tilt mechanism

The model of Figure 7 was simulated in time. The simulations explored the sensitivity to different integration times of the tip/tilt segment guider, controller gain, and latency.

The modeling process started with different integration times for the segment guider ranging from 50 Hz to 200 Hz, and with latencies equal to one frame and lower. The latency it is considered from when the exposure ends until the new position demand is received by the FSM controller. This includes the time it takes the camera to output the frame through the communication channel, the centroid calculation, coordinates transformation, control effort computation and communication time to deliver the new demand to the FSM controller.

The sensitivity to the wind disturbance input (or any other source) for the nominal case are shown in Figure 9. Lower gains are drawn with darker color lines; higher gains with lighter lines. The gains used to generate these plots were 0.013 (darkest) 0.063, 0.125, 0.188, 0.250, 0.313, 0.375, 0.438, 0.5, 0.625 (lightest).

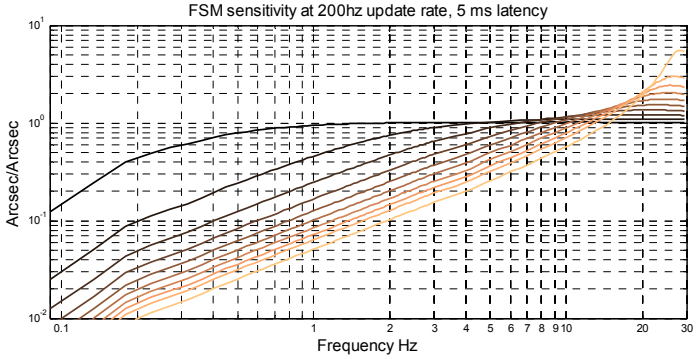

Figure 9. FSM closed loop sensitivity at 200 Hz guider update and 5 ms latency

3.7 Wind disturbance modeling.

Extensive site testing has provided statistical models that describe the mean wind speed and direction in a variety of scenarios. From this data, design specifications have been derived for the range of mean wind velocities for which the telescope is required to meet its performance specifications. CFD models were generated for several cases of enclosure orientation relative to the incoming wind, wind velocity, and enclosure opening configurations. The primary mirror assemblies were included in the CFD model, but the secondary support truss and top end were excluded for simplification. The results from these CFD models included flow velocities and pressures within the enclosure.

3.7.1 Static analysis

For wind disturbances, the CFD generated distribution of velocities within the enclosure was used to obtain drag forces on the slender beam elements of the secondary support truss, top end, and secondary assemblies. Pressures calculated on the primary mirror assemblies in the CFD model were directly mapped onto the corresponding plate and shell elements in the FEM. These pressures and forces were then applied as load to the FEM in a static or dynamic solution sequence to determine the LOS image motions and focus shift.

CFD model pressures were mapped onto the FEM. Pressures from the CFD model are the total pressure due to the uniform internal enclosure pressure and the wind velocity pressure. The uniform internal enclosure pressure is due to the pressurization of the enclosure due to a restriction of the vented air flow. The CFD solver (Star-CCM) does not allow for separation of enclosure pressure and wind velocity pressure in the output results. The dynamics of the structure will only be excited by the pressures caused by wind velocity. Enclosure pressure for each load case is estimated by examining the velocity profile. At locations where the velocity is equal to zero, the pressure due to wind velocity is also zero, leaving only the enclosure pressure. For each load case, a location showing zero velocity is chosen as close to the primary mirror as possible. The total pressure at this location is determined and is used as the enclosure pressure for the load case. This enclosure pressure is then subtracted from all the pressures mapped from the CFD model to the FEM. In this manner, only the wind velocity pressure remains.

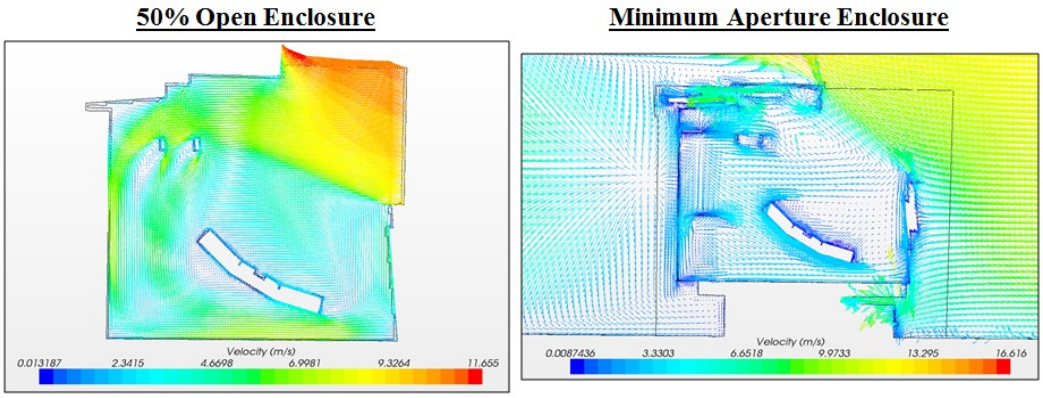

Figure 10 CFD Wind Velocity for 50% Open Enclosure and Minimum Aperture Enclosure

A cross-section of the wind velocity through the primary mirror is shown in Figure 10 for the 50% open enclosure (all vents at 50% open) and the minimum aperture enclosure (all vents closed) configurations. The stagnation point for the minimum aperture enclosure is directly above the primary mirror. The stagnation point for the 50% open enclosure is behind the primary mirror. This leads to much higher wind velocities and pressures on the front surface of the primary mirror for the 50% open enclosure load case. The mapped pressures on the primary mirror are shown in Figure 11. The scales of the contours have been adjusted in order to highlight the areas of high and low pressure.

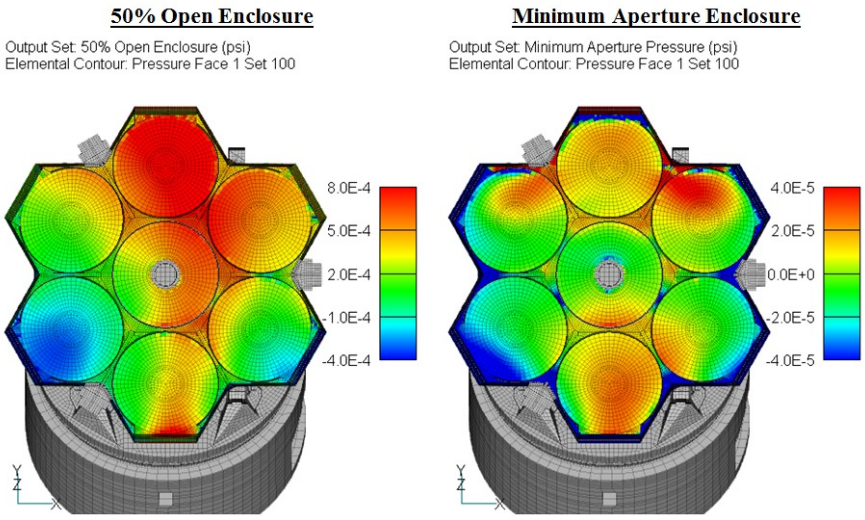

Figure 11 . CFD Wind Pressure for 50% Open Enclosure and Minimum Aperture Enclosure

Pressures on the primary mirror assembly are broken up into separate load cases or "patches" in order to define which sections of the FEM are correlated or uncorrelated for the dynamic analysis. Elements within a given patch are correlated, but one patch to another patch is uncorrelated. Patch size is selected to be as large as possible while still directly exciting critical modes. Selected patch sizes are larger than the apparent correlation length seen in the Gemini test data, making this model more conservative than selecting patches the same size as Gemini data. The secondary support truss geometry was mapped appropriately into the enclosure volume, and velocities at the locations were identified and used to generate the drag forces on the telescope structural elements.

3.7.2 Dynamic Component of the Wind Velocity

To characterize the dynamic component of the wind velocity on the GMT structure, the time series pressures and velocities are used to generate power spectral densities (PSD) of pressure and force (based on velocity squared). Pressure time history data from two sensors near the Gemini primary mirror is used to calculate an average pressure PSD. The average wind speed at the Gemini primary mirror is 2.9 m/s. The average wind speed in the GMT CFD model at similar primary mirror locations is 7.2 m/s. The average Gemini pressure PSD is scaled up by the ratio of wind velocities (7.2 m/s to 2.9 m/s). The resulting GMT pressure PSD follows a Kolmogorov fit as described in *Characterization of Wind Loading of Telescopes* by Angeli et al[3] and shown below using constants C_{pt}^{vK} = 1.3e3 Pa^2/Hz and f_0 = 0.209 Hz.

$$\Phi_{pt}^{vK} = \frac{C_{pt}^{vK}}{\left[1+\left(\frac{f}{f_0}\right)^2\right]^{7/6}}$$ [Equation for Kolmogorov fit]

The Kolmogorov PSD is then normalized by the pressure at low frequency. The final GMT pressure PSD shown in Figure 12 is used as a dynamic PSD scaling function for the pressures mapped to the primary mirror segments and cells.

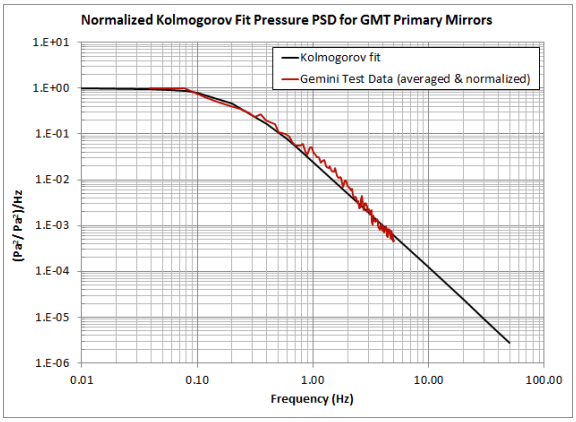

Figure 12. Normalized Kolmogorov fit pressure PSD for GMT primary mirrors

For the secondary support truss and the Top End, drag forces are calculated from the GMT CFD velocities. The dynamic scaling function for forces is based upon the velocities measured at the secondary mirror from the Gemini test data. For the cases selected, a normalized velocity squared spectrum was calculated by computing the velocity squared spectral density for each data set, and then dividing that spectrum by its associated mean squared velocity. All relevant cases from the Gemini data were considered and a design envelope over these results was used for the specification of dynamic forces to the secondary support truss and the Top End.

The derivation of the normalized velocity squared spectrum and the drag force spectrum are given below.

$$psd\ V^2_{norm} = \frac{psd\ V^2_{M2}}{V^2_{mean}}$$

Where:

$psd\ V^2_{norm}$ = the normalized velocity spectral density $((m/s)^2/(m/s)^2)/Hz$

$psd\ V^2_{M2}$ = the velocity squared spectral density calculated from the time series data measured at the M2 anemometer $(m/s)^2/Hz$.

V^2_{mean} = The mean squared velocity $(m/s)^2$

Random vibration force spectral densities applied to the beam elements in the FEM is computed as follows:

$$psd\ F_{drag} = \left(\frac{1}{2}\,\rho\, C_d\, A\right)^2 V^2_{mean}\,(psd\ V^2_{norm})$$

Where:

$psd\ F_{drag}$ = The force spectral density applied to the beam elements in the model (N^2/Hz)

ρ = The mass density of air at the site elevation (kg/m^3)

C_d = The drag coefficient of the beam

A = The area of the beam element facing the wind (m^2)

V^2_{mean} = The mean squared velocity from the CFD model $(m/s)^2$

$psd\ V^2_{norm}$ = The normalized velocity power spectral density $((m/s)^2/(m/s)^2)/Hz$

All of these normalized spectra were plotted and the envelope over these spectra was used in the analysis. A plot showing these normalized spectra and the envelope used in the simulation is given in Figure 13. The data sets are identified by their designated name and listed in the legend. The names correspond to the Gemini test data sets found in

the link (http://www.gsmt.noao.edu/studies/wind_tests1/index.html). These normalized spectra were then used to scale the forces applied to the secondary support truss and the Top End.

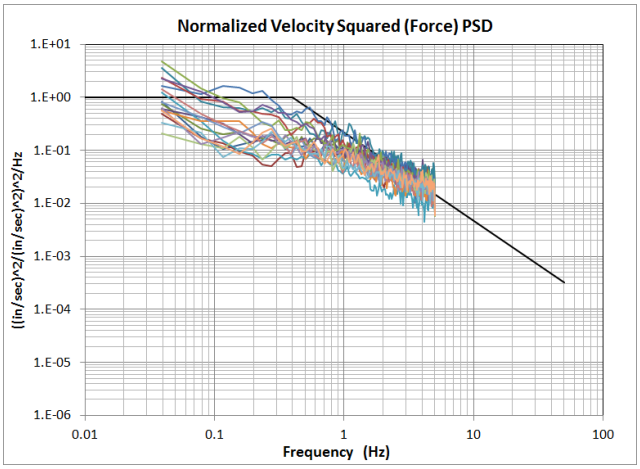

Figure 13. Normalized Velocity Squared (Force) PSD for secondary support truss and Top End.

3.7.3 Analysis Cases

Several analysis cases were considered. However, only the dynamic analysis results for the 50% open enclosure and minimum aperture enclosure, cases C and D, are included in this paper, for this cases two wind directions were considered; telescope pointing into the wind, and 50 degrees away from the wind.

1. Telescope pointed into the wind at a zenith angle of 30 degrees. The vent-gates and shutters are 50% open and the external mean wind velocity is 10 m/s (referred to as case C0 in the results below).
2. Telescope pointed away from the wind by 50 degrees, at a zenith angle of 30 degrees. The vent-gates and shutters are 50% open and the external mean wind velocity is 10 m/s (case C50).
3. Telescope pointed into the wind at a zenith angle of 30 degrees. The vent-gates are closed and shutters provide a minimum aperture. The external mean wind velocity is 10 m/s (case D0).
4. Telescope pointed away from the wind by 50 degrees, at a zenith angle of 30 degrees. The vent-gates are closed and shutters provide a minimum aperture. The external mean wind velocity is 10 m/s (case D50).

Analysis used locked elevation and azimuth rotors. The pressure and force patches are analyzed uncorrelated within a random vibration solution sequence in NX/Nastran 8.5. The results were calculated for 0.1 Hz to 50 Hz. Modal damping was set at 2% of critical for all of the analysis cases. The locked rotor PSD signals were calculated for the Azimuth and Elevation Axis. Focal plane image motion PSD signals were computed for X and Y axis at the Direct Gregorian Narrow Field focal plane. Focal shift was also computed, but it is not reported here. Image motion was computed at folded ports, but not presented here, because it difference to the DGNF were below 0.001 arcsec RMS, therefore the results of this paper applies for all focal planes.

4 MOUNT WIND RESPONSE

The results of the windshake modeling are inserted as disturbances on the control diagram of Figure 14. The lock rotor response to windshake is inserted as a disturbance to the input of the plant (Tw) and the image motion of each subaperture is introduced as a disturbance to the output of the plant. The torque disturbance over the axes is rejected by the position control loop, the residual signal Tm will excite the focal plane response, this response is added to the locked rotor image motion response. The added results correspond to the focal plane image motion with mount control but no tip/tilt control. Once the tip/tilt control is enabled, the final focal plane image motion is computed. The contribution of

each subaperture is scaled by the contribution of the relative reflective area of that subaperture. The figure of merit for the focal plane image motion induced by the wind is measured in arcsec RMS.

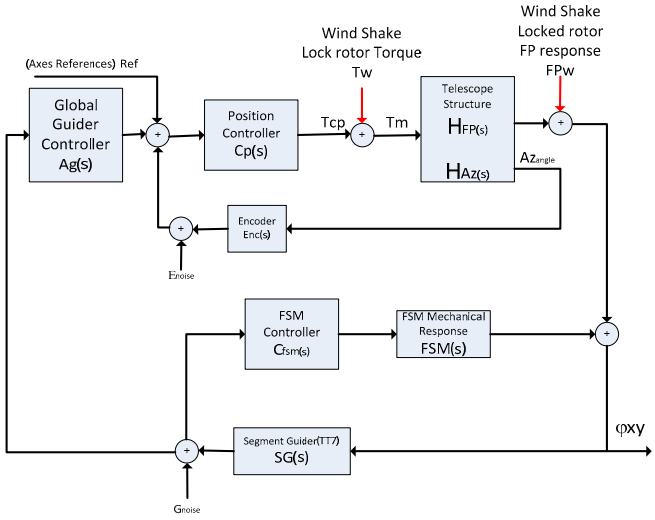

Figure 14. Mount control block diagram

For each axis the torque imprinted by the wind will be rejected by Tm=Sio*Tw, where Sio was previously defined, for each axis.

The plot in Figure 15 shows the cumulative forward sum at the drives of each axis of the locked rotor response. The curves in dashed lines represent the attenuated torque (Tm) provided by the position control. It can be seen clearly on the plot the effect of the control loop rejecting the disturbances very well below 1 Hz, which is the objective of the mount.

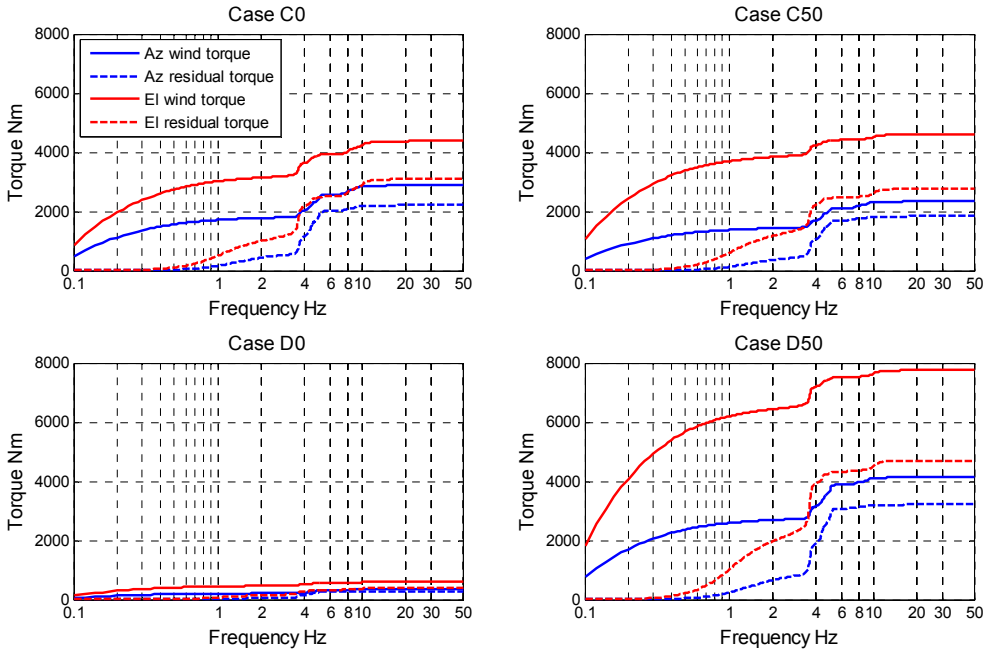

Figure 15 . Torque rejection by the mount control.

The torque Tm is scaled by the torque to focal plane transfer function of the telescope (Ht) and adding the locked rotor image motion we obtain the total image motion when the mount control is active but the tip/tilt control is inactive. There is a small rejection at low frequencies introduced by the Global Guider that was not taking into account in this analysis. The Global Guider will offload the "average global" tip and tilt from the segmented guider to the mount.

Figure 16 presents cumulative RMS focal plane image motion in X and Y axis for the four wind cases.

FPxy=Ht*Si*Tw+FPxylr

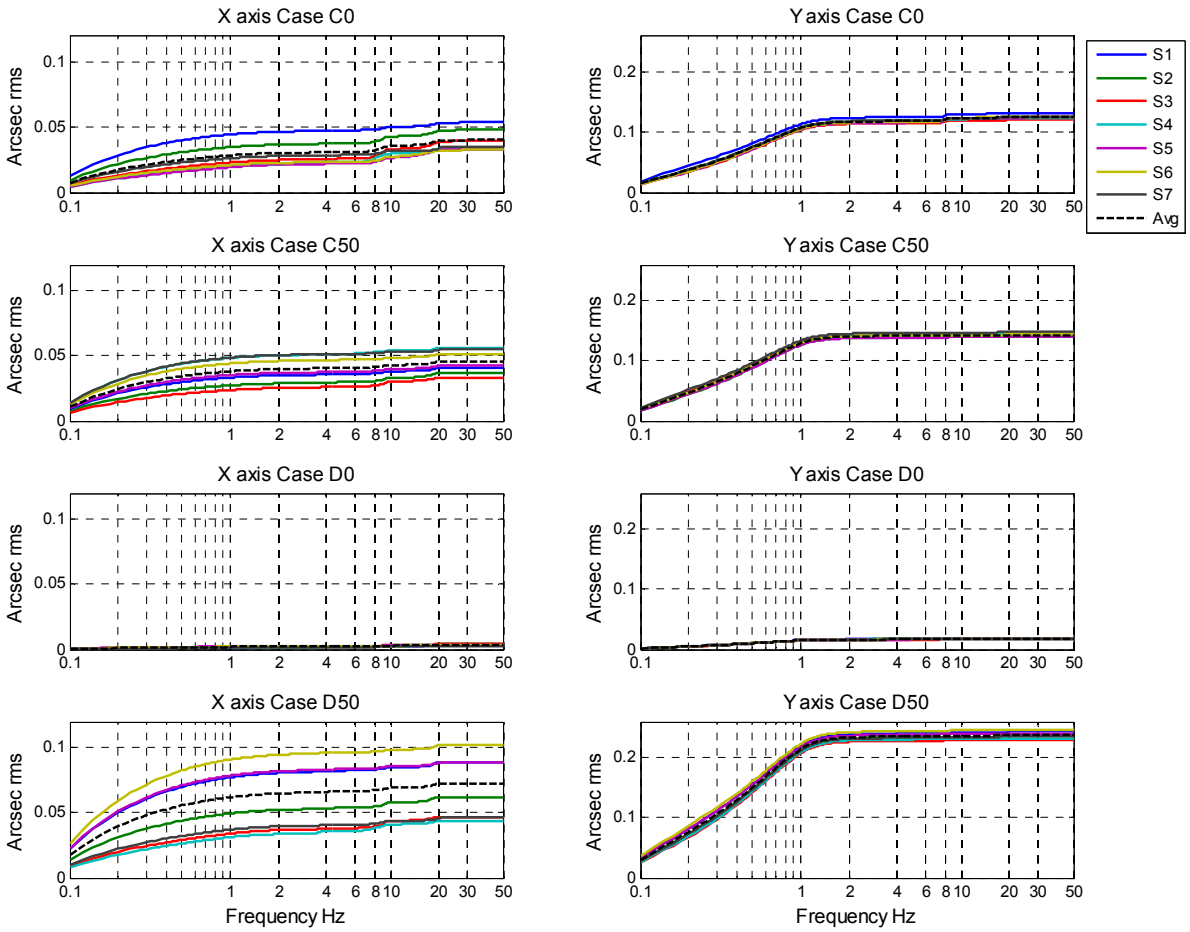

Figure 16 . Focal plane image motion per subaperture after mount control

For easy comparisons all the wind cases are plotted at the scale per axis. Note the difference of 1:2 from the X axis to the Y axis.

Looking at the cumulative plots, it is clear that without the use of the tip/tilt control only case D0 will meet the budget of 0.043 arcsec RMS. Interestingly, case D50 exhibits the largest amount of motion. The CFD analysis revealed that a totally closed enclosure will develop a vortex, because there is no "escape route" for the wind. The total focal plane image motion developed in cases C50 and C0 are comparable, and it is clear that the image motion is dominated by the global motion of the Y axis.

The tip/tilt control provides independent rejection per sub aperture and per axis at higher bandwidth than the mount can as detailed previously. The residual motion is fed to the rejection transfer function of the tip/tilt system providing the final image motion. The seven sub apertures motions are combined and scaled by their proportional light collecting area and added in quadrature to obtain the final image motion value.

$$\mathrm{FPx} = \frac{\mathrm{FPfsmx7}}{8.264} + \sum_{i=1}^{6} \frac{\mathrm{FPfsmxi}}{6.826} \qquad \mathrm{FPy} = \frac{\mathrm{FPfsmy7}}{8.264} + \sum_{i=1}^{6} \frac{\mathrm{FPfsmyi}}{6.826}$$

Figure 17 presents the cumulative focal plane image motion in arcsec RMS after the tip/tilt control. Just from looking at the images it seems that the case C50 might meet the budget. Final numbers are presented on Table 1.

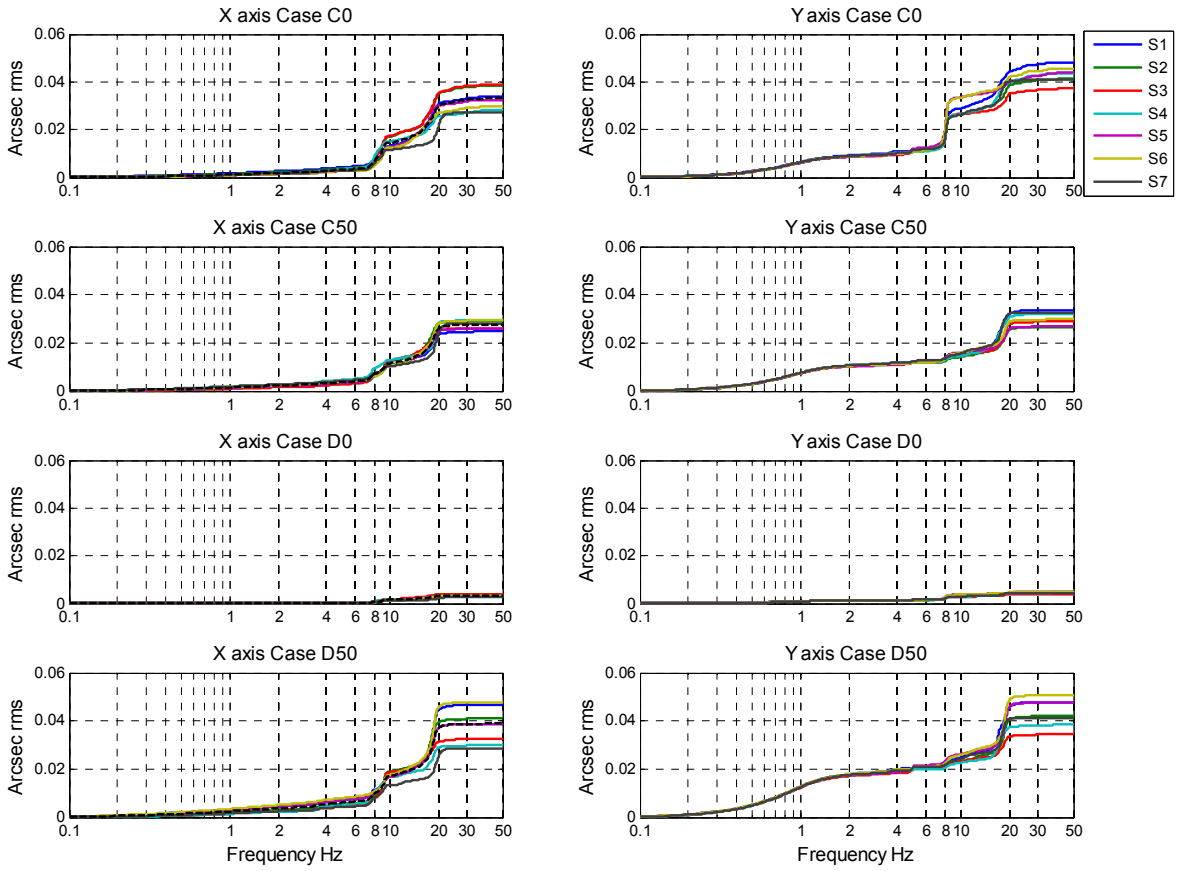

Figure 17. Segment focal plane image motion after tip/tilt Correction

5 RESULTS

Results for four wind scenarios were compiled in Table 1. For this table a tip/tilt control integration gain of 0.188 was used, which produces -3dB bandwidth close of 10Hz. The total budget allocation for the wind disturbance on the focal plane is only 0.043 arcsec RMS, two of four selected cases meet requirement.

Table 1 . Windshake results.

	Total focal plane image motion (arcsec RMS)		
Wind Scenario	Axis X	Axis Y	Total
C0	0.031	0.047	0.057
C50	0.026	0.032	0.041
D0	0.003	0.005	0.006
D50	0.037	0.048	0.061

Increasing the bandwidth of the tip/tilt control system will increase the rejection of the wind disturbance at lower frequencies, at the cost of amplifying the error above the crossover frequency, as it is shown in rejection curves of Figure 9. At the same time propagation to the focal plane of the centroid calculation error (noise) is increased. In order to explore the sensitivity of the focal plane image motion to the tip/tilt control bandwidth the results of table 2 were prepared. The residual focal plane image motion is compared against the combination of the two budgets, the budget for the centroid calculation is 0.039 arcsec RMS and the wind disturbance budget is 0.043 arcsec RMS, the total combined budget is 0.058 arcsec RMS. The centroid error is modeled as a white noise of 0.028 arcsec RMS per axis, this white noise in band limited to 100Hz, which corresponds to the Nyquist frequency of the sampled data from the segmented guider. The centroid noise is filtered by the tip/tilt closed loop, see Figure 7, due to the low bandwidth of the system. Using the model of Figure 7, the centroid error effect on the focal plane can be easily evaluated to the different tip/tilt Bandwidth. The resulting value is added to the focal plane image motion according to:

$$IM = \sqrt{Tip/Tilt_{residual}^2 + 2 * Error_{Centroid}^2}$$

Where IM is the total image motion, considering centroid noise propagation.

Tip/tilt Residual is the residual image motion at the focal plane computed in the last column of Table 1.

Error $_{Centroid}$ is the propagation of the centroid error to the focal plane of a single axis.

In Table 2 the total focal plane image motion is computed for the four wind cases and for different tip/tilt Bandwidths, the bold values indicate when the budget is met. Notice that an optimum is reached about 10Hz (which corresponds to 0.187 controller gain). It is also clear that case C0 and D50 are also very close to meeting the requirements and it is expected that they would be below the requirement with adjustment of the enclosure vents gates.

Table 2. Focal plan image motion in arcsec RMS sensitivity to tip/tilt bandwidth

	Tip/Tilt bandwidth				
Wind Cases	2.5 Hz	5 Hz	10 Hz	17.5 Hz	30 Hz
C0	0.068	0.061	0.059	0.059	0.060
C50	0.061	**0.047**	**0.044**	**0.046**	**0.048**
D0	**0.011**	**0.014**	**0.017**	**0.022**	**0.026**
D50	0.097	0.079	0.063	0.062	0.075

6 CONCLUSIONS

Under the current modeling of the wind, the focal plane image motion induce by the wind will depend on the delicate balance of the vent gates configuration and wind orientation. Table 1 shows the telescope mount along with the Tip/Tilt control system will meet a budget of 0.058 arcsec RMS under 10 m/s environmental wind speed, which represents 75%

percentile of the wind speed at the site. Further modeling is required to understand the performance under different wind angles and vent opening configurations.

From the tip/tilt control system it can be seen that an optimal performance is reached when the integration gain of the system is about 0.188 (or 10 Hz bandwidth), this is largely due the amount of disturbance in the frequency range 10-40 Hz.

It is clear too from the image in Figure 17 that one of the limitations of the system is the excessive torque on the Elevation axis, which dominates the Y axis motion. This excessive torque can be better rejected using a different control algorithm, or just by blocking the wind load with the vent gates configuration.

The limitations of the tip/tilt system, can be observed on the disturbance rejections curves of Figure 9. In order to achieve a good rejection at low frequencies an amplification of the high frequencies disturbances is a payback. Lower latencies of the feedback system will achieve close to null amplification above 20 Hz, while keeping the same attenuation at lower bandwidths, but this will require a change in the selected camera and optics for the segmented Guider (TT7).

ACKNOWLEDGEMENTS

This work has been supported by the GMTO Corporation, a non-profit organization operated on behalf of an international consortium of universities and institutions: Astronomy Australia Ltd, the Australian National University, the Carnegie Institution for Science, Harvard University, the Korea Astronomy and Space Science Institute, the Smithsonian Institution, The University of Texas at Austin, Texas A&M University, University of Arizona and University of Chicago.

REFERENCES

[1] Johns et al , “Design of the Giant Magellan Telescope”, Proc SPIE 9145-50 (2014)
[2] GMT Corp, “Natural Seeing Image Quality Budget”, (GMT-SE-REF-00145),(2013).
[3] George Z. Angeli, Myung K. Cho, Mike Sheehan, Larry M. Stepp, “Characterization of Wind Loading of Telescopes”, Proc SPIE 4757:72-83 (2002)